Enabling Cooperative Autonomous Driving through mmWave and Reconfigurable Intelligent Surfaces

Michele Segata*, Marios Lestas†, Paolo Casari*, Taqwa Saeed‡,
Dimitrios Tyrovolas§, George Karagiannidis§, Christos Liaskos¶

*Department of Information Engineering and Computer Science – University of Trento, Italy
†Dept. of Electrical Engineering – Frederick University, Cyprus
‡School of Information Technology – Halmstad University, Sweden
§Dept. of Electrical Engineering – Aristotle University of Thessaloniki, Greece
¶Dept. of Computer Science and Engineering – University of Ioannina, Greece

Abstract*—Future cooperative autonomous vehicles will be able to organize into flexible platoons to improve both the efficiency and the safety of driving. However, platooning requires dependable coordination through the periodic wireless exchange of control messages. Therefore, challenging propagation scenarios as found, e.g., in dense urban areas, may hinder coordination and thus, lead to undesirable vehicle behavior. While reconfigurable intelligent surfaces (RISs) have been advocated as a solution to improper coverage issues, no system-level simulation exists that accounts for realistic road mobility and communication aspects. To this end, we present one such simulator built on top of the OMNeT++-based PLEXE and Veins frameworks. Specifically, our contribution is a simulator that takes into account vehicle mobility, physical layer propagation, RIS coding, and networking protocols. To test our simulator, we implement an RIS-assisted autonomous platoon merging maneuver happening at an intersection where the absence of any RIS would limit successful packet exchanges to an area dangerously close to the intersection itself. Our results validate the simulator as a feasible tool for system-level RIS-assisted cooperative autonomous vehicle maneuvering, and ultimately show the benefit of RIS as roadside infrastructure for wireless coverage extension.

I. INTRODUCTION

Existing wireless technologies, such as direct short range communications (DSRC) for vehicular scenarios [1] have been well established to serve cooperative safety applications. Yet, they are susceptible to blockages [2], which constitute a significant impairment for smooth and timely data exchanges, especially in emergency situations. This is exacerbated in the millimeter wave (mmWave) bands, which are currently being considered to overcome the bandwidth scarcity for next-generation networks and the speed limitations of the DSRC and long term evolution (LTE) technologies. However, mmWave communications mostly rely on comparatively large arrays to achieve directional radiation. This solution improves link quality in static deployments, but makes link maintenance and device tracking very challenging in fast mobility scenarios, often resulting in non-line of sight (NLOS) channels and degraded performance [3]. Therefore, supporting vehicular communications at mmWave frequencies requires technology that can help reduce the likelihood of link breakage and NLOS communications.

One such technology is reconfigurable intelligent surfaces (RISs) [4], [5], which can offer artificial LOS paths in NLOS scenarios. The performance improvement obtained in vehicular communication scenarios thanks to RISs was demonstrated by NTT DOCOMO in Japan back in 2018 [6]. One of the most promising enabling technologies for RIS implementation are metasurfaces, where due to sub-wavelength apertures, they can precisely control the impinging electromagnetic waves to realize multiple array functionalities including steering and diffusion [7]. In more detail, the densely packed unit cells of the metasurfaces, are periodically placed over a substrate and by tuning their complex impedance, it becomes possible to control the surface currents induced on the metasurface and thus enable a desired scattering diagram. Such tuning can be achieved through varactors and varistors, or by constructing the unit cells from appropriate materials such as nematic liquid crystals [8], [9].

For vehicular communication scenarios, RISs have been considered in a number of recent works [10], focusing mostly on the challenging aspect of preserving communication reliability in fast mobility conditions. For example, a robust transmission scheme for vehicular communication was proposed in [11], while an outage analysis was offered in [12]. Furthermore, various RIS designs for vehicular applications have been reported [13], [14], and the optimal RIS placement problem has been addressed in, e.g., [15]. Moreover, communication aspects that can affect the switching strategy, such as reconfiguration delays and power consumption, have been recently investigated in [16], while security issues have also received attention recently [17].

Even though metasurfaces are gaining momentum, there currently exist no system-level simulation tools that can account both for realistic road mobility and for communication aspects. In this respect, the literature is limited to a few works such as [18]. Even in this case, the simulation framework therein does not account for autonomous driving applications. As such, an in-depth analysis of the advantages RISs bring to autonomous driving performance is still missing in the existing literature. In addition, the results in [18] rely on an early propagation and path loss model that does not consider the

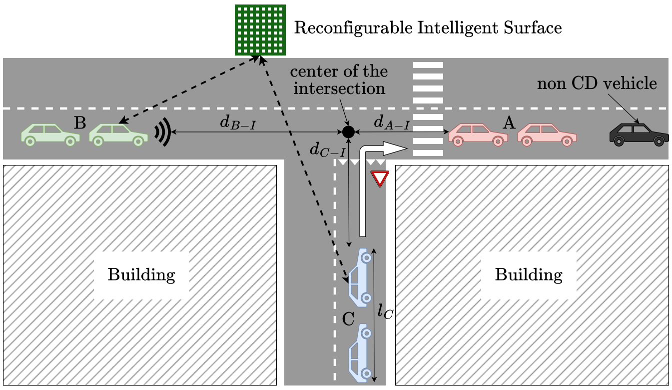

Figure 1. Cooperative intersection merging scenario.

metasurface coding procedure.

From the above discussion, we observe that the integration of RISs in autonomous driving applications, although potentially beneficial, has not been specifically investigated in the literature from a performance evaluation and protocol design perspective. Specifically, due to the fact that RISs are being widely accepted as an enabling technology for 6G and future vehicular communication systems, it becomes crucial to develop a simulation framework that complements autonomous driving, vehicular mobility and networking features with recent findings in RIS modeling. Such a framework aims to serve as a realistic tool for the performance evaluation of RIS-assisted autonomous driving applications. To the best of our knowledge, this paper presents the first step towards the development of such a tool by integrating the metasurface coding procedure utilized in previous RIS-related work, within the PLEXE simulator [19]. We first validate the current implementation by comparing it against previously published results. Then, we consider an RIS-assisted, platoon merging scenario at an intersection as a showcase of the effectiveness of the developed tool.

The remainder of this paper is organized as follows. In Section II we describe the cooperative driving (CD) scenario we consider, implemented in PLEXE [19] and Veins [20]. Section III introduces our communication model and the metasurface coding procedure. Section IV presents simulation results. Finally, we draw concluding remarks and describe future work in Section V.

II. Cooperative Driving Scenario

To show the potential of RISs for CD, we consider a cooperative intersection merging maneuver. Fig. 1 shows a sketch of this scenario, a T-shaped intersection where cooperative autonomous vehicles (CAVs) coming from the bottom (group C) need to turn right and merge into the main traffic flow. On the side of the road, we have buildings that obstruct visibility and block LOS communications, impairing the use of cameras and of classic vehicular communication technologies such as IEEE 802.11p. We assume that, for human-driven vehicles, the traffic coming from the bottom road should yield the right of way to vehicles traveling left to right but. However, in a CD scenario, it might be more efficient to coordinate the traffic so that vehicles in group C merge in between groups A and B, if inter-vehicle gaps so allow. This may avoid that vehicles in group C come to a complete stop, and should only very slightly slow down vehicles in group B.

From now on, we assume that all groups A, B and C are in fact vehicle platoons, and that slowing down platoon B to let platoon C merge in is always the most efficient action.[1] We also assume that all platoons to be driven by the PATH cooperative adaptive cruise control (CACC) algorithm [21], which maintains a constant inter-vehicle gap between the vehicles. To perform the maneuver, vehicles in platoon C need to know the distance to the last vehicle in platoon A in order to properly regulate their speed and smoothly merge in the intersection. The driving pattern of platoon A might be disturbed by other, non-cooperative vehicles, as depicted in Fig. 1. Such information can be shared by the leader of platoon B, which has a clear LOS towards platoon A.

To share such information, we consider a cooperative perception (CP) approach, whereby the leader of platoon B shares raw sensor data with the leader of platoon C, instead of data post-processing results (e.g., distance measurements). The reasons is that vehicles can build a more complete view of the surrounding environment, especially when the LOS is obstructed [22], [23]. In our example, not only can vehicles in platoon C be aware of the distance to platoon A, but by receiving raw data such as the camera video stream, they can become aware of vulnerable road users (VRUs) behind the corner (see the zebra crossing in Fig. 1). In this specific scenario, the use of RISs in the mmWave spectrum can be extremely beneficial because they can overcome the missing LOS problem, as well as providing large bandwidths, necessary to stream raw sensor data.

To formally describe the maneuver, we first introduce the CACC control law employed by the CAV [21]:

$$u_i^{\text{CACC}} = \alpha_1 u_{i-1} + \alpha_2 u_0 + \alpha_3 (v_i - v_{i-1}) + \alpha_4 (v_i - v_0) + \alpha_5 (-d_i + d_d). \tag{1}$$

In Eq. (1) u_i^{CACC} is the desired acceleration of vehicle i (i.e., prior to actuation), v_i represents the speed of vehicle i, while d_i and d_d represent the measured and the desired inter-vehicle distance, respectively. The control gains α_i are defined as

$$\begin{aligned} &\alpha_1 = 1 - C_1; \quad \alpha_2 = C_1; \quad \alpha_5 = -\omega_n^2 \\ &\alpha_3 = -\left(2\xi - C_1\left(\xi + \sqrt{\xi^2 - 1}\right)\right)\omega_n \\ &\alpha_4 = -C_1\left(\xi + \sqrt{\xi^2 - 1}\right)\omega_n, \end{aligned} \tag{2}$$

where C_1 weights the leading and preceding vehicles accelerations, while ξ and ω_n set the damping ratio and the bandwidth, respectively.

Intuitively, Eq. (1) uses the leading and preceding vehicles' acceleration and speed as well as the distance to the preceding

[1] If group B is close to platoon A, letting platoon C merge in between may require platoon B to completely stop, but the complete design and optimization of a merging maneuver is outside the scope of this paper.

vehicle to compute the acceleration/deceleration command to maintain the desired distance d_d. The set of vehicles in the platoon from which a member takes control information is defined as the information flow topology (IFT). In Eq. (1), the CACC uses a leader- and predecessor-following IFT.

To implement the maneuver, we consider the following quantities:

- d_{A-I}: the distance from the center of the intersection to the last vehicle in platoon A;
- d_{B-I}: the distance of the leader of platoon B to the center of the intersection;
- d_{C-I}: the distance of the leader of platoon C to the center of the intersection;
- l_C: the length of platoon C.

To compute their control actions, the leaders of platoons B and C should feed to the control algorithm a different measured distance d_i. In particular, platoon B should consider the distance $d_i = d_{A-I} + d_{B-I} - l_C$, i.e., leaving room for platoon C to merge in. Group C, instead, needs to consider $d_i = d_{C-I} + d_{A-I}$, i.e., the distance to the center of the intersection plus the distance to platoon A. By acting on the measured distance, the platoons automatically adjust their distances to match the desired one.

However, the above setup is suboptimal, because the vehicles might implement unnecessary control actions. Consider for example the case in which the gap between platoons A and B is already large enough to merge platoon C in. As a result, platoon B will accelerate to compensate for the distance error, because $d_d < d_i$. Such unnecessary acceleration wastes fuel Moreover, the system should only decelerate if there is no room for platoon C. To overcome these problems, we assume the leader to run multiple control algorithms in parallel, coupling the CACC with a standard cruise control (CC) with control function

$$u_i^{\text{CC}} = k_p \left(v_d - v_i \right). \tag{3}$$

In Eq. (3), v_d is the desired speed, while k_p the proportional control gain. For the leaders, the final control law is defined as

$$u_i = \min \left(u_i^{\text{CC}}, u_i^{\text{CACC}} \right). \tag{4}$$

Eq. (4) causes the leaders to accelerate only if their current speed is lower than the desired one, but always maintaining a distance larger than d_d, thanks to the CACC.

One important detail is how to set the leader and the predecessor for each vehicle. Define each platoon as a set of vehicles, i.e.,

$$A = \{v_0^A, v_1^A, \ldots, v_{N_A-1}^A\} \tag{5}$$
$$B = \{v_0^B, v_1^B, \ldots, v_{N_B-1}^B\} \tag{6}$$
$$C = \{v_0^C, v_1^C, \ldots, v_{N_C-1}^C\} \tag{7}$$

For each member v_i^A of platoon A (except the leader), the choice of the leader and the predecessor is trivial, i.e., v_0^A and v_{i-1}^A, respectively. For the members of platoons B and C, we assume the same. The leaders of platoons B and C, instead, need to choose which vehicles to pick. In here, we assume the configuration in Fig. 2, i.e., the leaders choose as leader and predecessor the leader and the last vehicle of the platoon preceding them on the road, respectively. More formally v_0^C will pick v_0^A and $v_{N_A-1}^A$ as leader and predecessor, respectively, while v_0^B will pick v_0^C and $v_{N_C-1}^C$. This guarantees leaders of platoons B and C to properly follow as if they were a member of the platoon preceding them on the road.

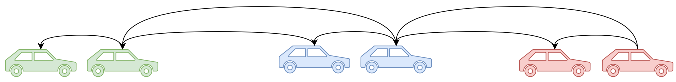

Figure 2. Information flow topology configuration.

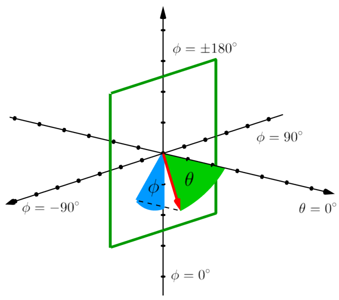

Figure 3. Graphical description of the coordinate system. The green square represents the metasurface.

The key issue now becomes how to get control data from platoon A to C, given the obstructed LOS. In this case, we assume the leader of platoon B to relay A's data to C through the RIS link. Data from platoon A to B is transmitted through a standard IEEE 802.11p link. In turn, the leader of platoon C can relay data about its members through the same RIS link to platoon B.

III. Communication Models

A. Directivity-Based Communication Model

The metasurface directivity is a property that measures the amount of energy radiated towards a specific direction. Therefore, the directivity highly relies on the scattering diagram of the surface which, in turn, is greatly affected by the metasurface parameters such as its size and number of unit cells. To understand the relationship between these elements it is essential to first explain the concept of metasurface coding [24].

1) Metasurface coding: Anomalous reflection is achieved through having a linear phase gradient, $\Phi(x, y)$, over the meta-atoms of the RIS. This implies that each meta-atom attains a specific phase based on its location (i.e., x,y coordinates) on the surface, the incidence angle and the reflection angle. The phase profile of the surface follows the momentum conservation law for wave vectors at the air-metasurface interface as expressed below:

$$\begin{aligned} k_i \sin\theta_i \cos\phi_i + \Phi'_x &= k_r \sin\theta_r \cos\phi_r, \\ k_i \sin\theta_i \sin\phi_i + \Phi'_y &= k_r \sin\theta_r \sin\phi_r, \end{aligned} \tag{8}$$

where Φ'_x and Φ'_y are the phase gradients along the x-axis and the y-axis, respectively. k_i and k_r, on the other hand, represent the incidence and reflection wave vectors, where azimuth ϕ

and elevation θ are as depicted in Fig. 3. Solving for Φ'_x and Φ'_y from Eq. (8), yields the overall phase gradient required to reflect a beam impinging from the incident angles $\{\theta_i, \phi_i\}$ towards the reflection angles $\{\theta_r, \phi_r\}$. The phase of a single meta-atom (i.e., unit cell) can then be found as follows:

$$\Phi_{ij} = (\Phi'_x i + \Phi'_y j)d_u - \Phi_{00}, \tag{9}$$

where Φ_{00} is an arbitrary phase (assumed to be 0 for simplicity), and i and j denote the number of row and column on which the respective unit cell lies. The phase profile of the surface defines the radiation pattern which is reflected (with respect to the receiver) in the directivity.

2) Communication model: Considering the scenario depicted in Fig. 1, the wave is transmitted from the transmitter vehicle to the RIS and then to the receiver vehicle. Hence, the communication channel gain can be expressed as follows:

$$G_{total} = G_T G_{RIS} G_R \tag{10}$$

where G_T, G_{RIS} and G_R denote the transmitter gain, the RIS gain and the receiver gain, respectively. The gain of the surface can then be expressed as follows [25]:

$$G_{RIS} = \epsilon D \tag{11}$$

where D represents the directivity [26] and ϵ the efficiency of the surface. We can thus express the received power strength at the receiver through the following equation

$$P_r = \frac{G_{total} P_t}{PL_{total}} \tag{12}$$

P_t denoting the transmitter power and PL the path loss which is generally defined as follows [27]:

$$PL = \left(\frac{4\pi f}{c}\right)^2 d^n \chi_\sigma \tag{13}$$

where f is the considered communication frequency, c is the speed of light, n is the path loss exponent, $\chi_\sigma \sim \mathcal{N}(0, \sigma^2)$ expresses the shadow fading effect defined by Gaussian distribution with zero mean and standard deviation σ, and d denotes the distance between any two consecutive nodes in the communication path. The total path loss can be expressed as

$$PL_{total} = PL_{T \to R \to D} = \left(\frac{4\pi f}{c}\right)^2 (d_1 + d_2)^n \chi_\sigma \tag{14}$$

where d_1 and d_2 represent the distances between the transmitter and the RIS, and the RIS and the receiver, respectively. Notice that the path loss is defined over the sum of the two distances d_1 and d_2. This is only correct if we operate in the near field of the RIS [28], otherwise we would need to consider the double path loss effect [5], i.e., the product of the distances. In here we assume a large RIS enabling to work in the near field of the antenna. In our future work we will consider smaller RIS with a larger number of elements, enabling higher gains to compensate for double path loss effects.

After computing the total path loss, the signal to noise ratio (SNR) at the receiver can be defined as usual:

$$SNR = \frac{P_r}{P_{noise}} \tag{15}$$

Given the SNR, we compute the probability of reception using the standard bit error rate curves for orthogonal frequency division multiplexing (OFDM) available in Veins [20].

IV. Results and analysis

In this section we show the performance evaluation in terms of validation of the implementation models as well as the potential benefits of RISs for CD applications, in particular by considering the scenario defined in Section II.

A. Far field pattern validation

We implement the model for RIS in [26], [29] as a module for Plexe [19]. Differently from past work [18] and as mentioned in the introduction, our implementation enables the possibility of considering the coding procedure, enabling dynamic reconfiguration of the metasurfaces. In addition, as the implementation is based on Plexe, it supports cooperative driving vehicles by definition. Currently the software is still in its infancy and needs further polishing before releasing it to the public. Part of our future work is clearly to release the framework as open source software, but this is not currently a contribution of this manuscript.

As a first step, we validate the implementation of the coding procedure and the computation of the far field pattern, which are fundamental to enable the reconfiguration of the RIS and compute the gain provided by the surface given the position of transmitter-receiver pairs. Fig. 4 shows four sample far field patterns. The RIS is coded for a normal incidence ($\theta_i = 0°$) and for the reflection angles indicated under each plot. We remind the reader that Fig. 3 shows the coordinate system that we consider. The azimuth angle ϕ is the angle measured by projecting the beam direction on the metasurface, spanning thus over $360°$, while the elevation is the angle measured between the beam direction and the normal to the surface, on the plane generated by the two vectors. By convention, $\theta = 0°$ indicates the normal to the surface, while $\theta = 90°$ indicates a beam parallel to the metasurface. We disregard the half-space behind the surface ($\theta > 90°$). With respect to the azimuth ϕ, if the metasurface is perpendicular to the ground as in Fig. 3, $\phi = 0°$ points towards the ground, $\phi = -90°$ points towards the right of the surface (looking in the direction of the normal), while $\phi = 90°$ points towards the left.

The far field is computed for a normal incidence and for the reflection angles on the axes ($\phi_r \in [-180°, 180°], \theta_r \in [0°, 90°]$), with a resolution of $1°$. The color value represents the gain on a linear scale.

The different shape of the patterns for different elevation angles is due to the “cartographic projection” of the semi-sphere in front of the RIS. By looking at incidence angles not located at the extremes (Fig. 4b) the surface shows a focused, circular-like reflection pattern, as shown in [29, Fig. 7]. For further confirmation, we plot the pattern in Fig. 4b on a normalized dB scale (Fig. 5) in the range between $-30\,\text{dB}$ and $0\,\text{dB}$ for a direct comparison with [26, Fig. 6]. The pattern in Fig. 5 perfectly matches the one in [26], confirming the correct implementation of the model.

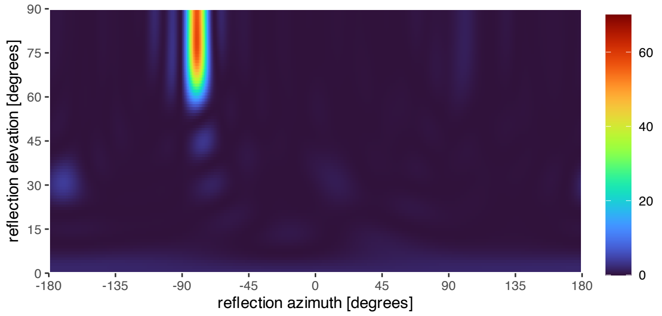

(a) $\phi_r = -80°, \theta_r = 80°$

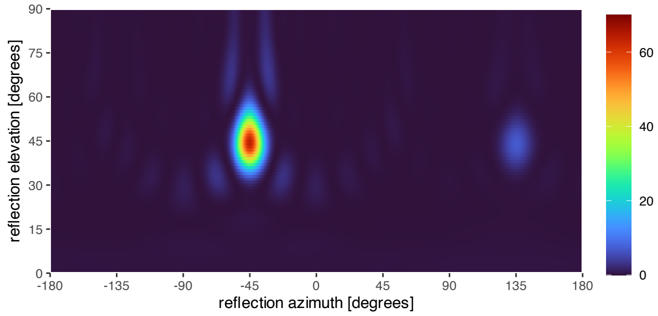

(b) $\phi_r = -45°, \theta_r = 45°$

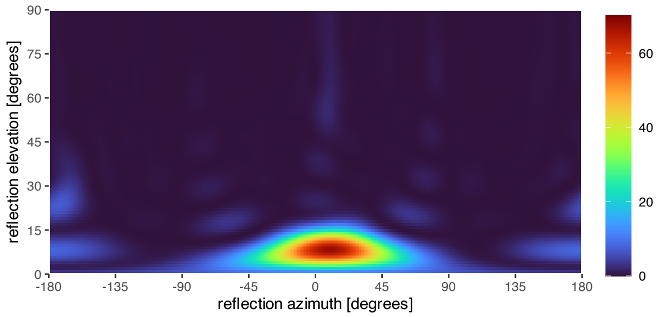

(c) $\phi_r = 10°, \theta_r = 10°$

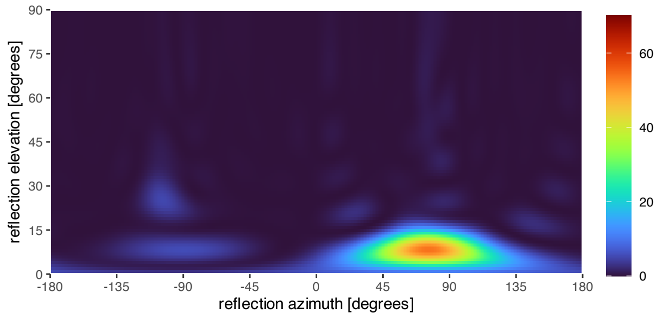

(d) $\phi_r = 75°, \theta_r = 10°$

Figure 4. Far field pattern for different reflection angles. The RIS is configured for the reflection angles indicated under the graphs and for normal incidence ($\phi_i = 0°, \theta_i = 0°$). The far field is computed considering a normal incidence and the reflection angles on the axes. The gain is on a linear scale.

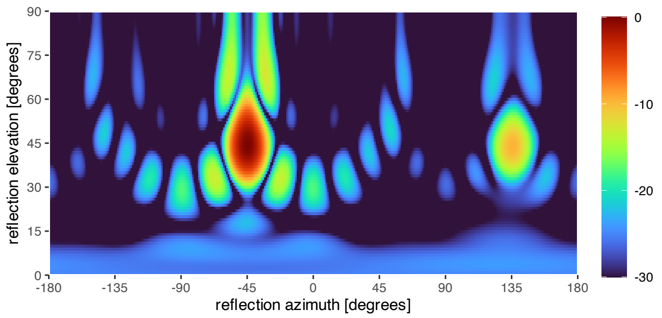

Figure 5. Far field pattern for normal incidence and $\phi_r = -45°, \theta_r = 45°$. The gain is on a normalized dB scale in the range from -30 dB to 0 dB for the sake of comparison with [26].

B. Channel model validation

After verifying the implementation of the far field pattern, we test the implementation of the channel model in a simplified scenario. The channel model is comprised of the far field model, the path loss model on the incident and reflected paths, plus the model computing incidence and reflection angles required for the far field model. We consider the intersection described in Fig. 1 with two vehicles only and without implementing any maneuver. We first run the simulation without communication, recording the positions of the vehicles over time. At simulation time 30 s we compute the incidence and reflection angles between the two vehicles considering the RIS to be positioned in the center of the intersection facing south. We code the RIS statically for such incidence and reflection angles and then re-run the simulation enabling communication between the two vehicles, in particular by having the vehicle coming from the south transmitting period messages to the other and recording the gain of the RIS as function of the position of the receiving vehicle. With respect to the model, we consider a center frequency of 25 GHz and a free space path loss with an exponent of 2.

Fig. 6 shows a screenshot of the simulation in SUMO at simulation time 30 s. Besides the intersection, the vehicles, and the buildings, our implementation draws the RIS in the scenario as a blue rectangle (not in scale) plus a projection of the path for which the RIS has been configured, enabling the user to visually inspect the simulation.

Fig. 7 shows the evolution of the gain, the total path loss, and the incidence and reflection angles as function of the distance to the intersection measured for the vehicle travelling west to east. With respect to the gain, the graph displays a step-like pattern which is due to the resolution of the far field pattern. The model is implemented analytically with a resolution of $1°$ for both the azimuth and the elevation angles. The resolution can clearly be increased at the expenses of the computational complexity. Alternatively, the gains could be pre-computed and stored in a lookup table, but we leave such optimizations as future work. Qualitatively, the gain starts from a relatively high value but continues to increase till roughly 100 m to the intersection, i.e., 30 s into the simulation as expected, corresponding to the position depicted in Fig. 6. After passing the optimal point,

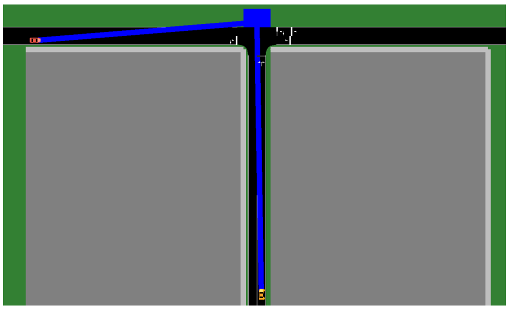

Figure 6. Screenshot of the validation scenario in the SUMO GUI with the RIS drawn as a blue rectangle together with the projection of the path for which the RIS has been configured.

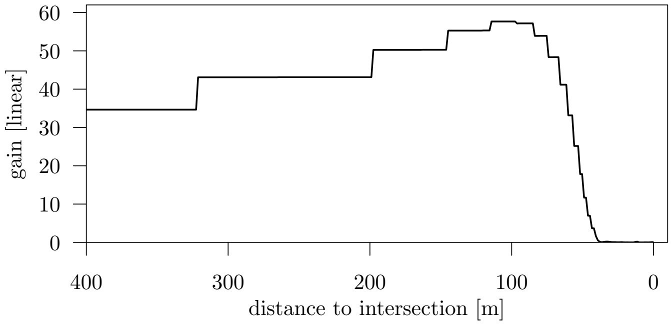

(a) RIS gain

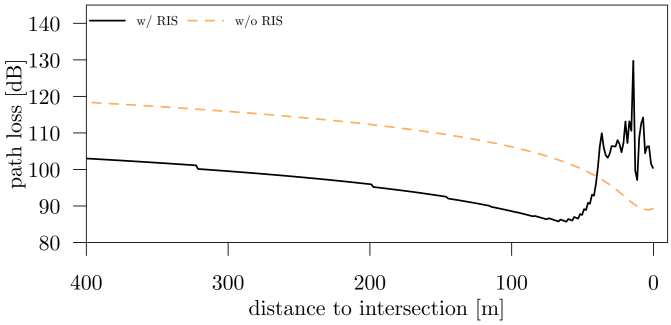

(b) total path loss considering incident and reflected path

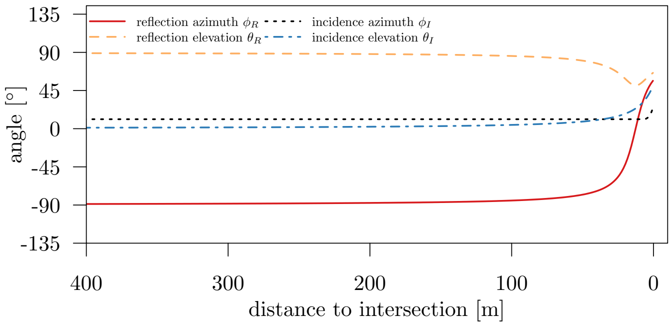

(c) measured angles

Figure 7. Evolution of the gain at the antenna, the total path loss, and the reflection and incidence angles w.r.t. distance to the intersection for the vehicle travelling west to east (receiver).

the gain quickly drops due to the changes in the incidence and reflection angles, especially the azimuth ϕ_r. Besides being a first validation of the implementation, these simple results already provide interesting insights. In a scenario like the one in Fig. 6, i.e., with straight roads, tracking errors can lead to suboptimal but still valid gains, at least when vehicles are far from the intersection. Tracking errors when vehicles come closer to the intersection might instead worsen the performance as incidence and reflection angles change more quickly. Still, by looking at the total path loss (Fig. 7b), we can see that the RIS in its optimal range provides more than $20\,\mathrm{dB}$ of gain. On the other hand, vehicles closer to the intersection would experience lower path losses. This suggests that tracking algorithms might focus their attention on vehicles closer to the intersection, as the intuition might also indicate.

C. Cooperative maneuvering scenario

In this section we consider the cooperative merging maneuver described in Section II. We first implement the maneuver in ideal conditions, i.e., using only IEEE 802.11p communication without the presence of buildings. This permits us to show the ideal maneuver dynamics. In a second scenario, we add a building close to the intersection, which causes the interruption of the communication between the leaders of platoons B and C for a certain period of time. Finally, to support the maneuver, we enable an additional mmWave link between such leaders to overcome the communication blockage thanks to the RIS. Table I summarizes network simulation parameters.

We start the discussion by first observing the ideal behavior. Fig. 8a shows the acceleration dynamics for the leaders of platoons A, B, and C, while Fig. 9a the virtual distance as computed by the leaders of platoons B and C, i.e., the distance of leader C to the last vehicle in A and the distance of leader B to the last vehicle in C, as depicted in Fig. 1.

With respect to the acceleration profiles, the changes in speed are due to the human driven vehicle in front of platoon A which induces traffic perturbations. Thanks to data sharing, all the leaders are capable of adapting to such changes, especially leader C, which is aware of such perturbations thanks to CP, i.e., leader B forwarding radar information to leader C.

With respect to the maneuver, we first need to mention that the minimum target inter-vehicle distance is $5\,\mathrm{m}$, i.e., vehicles will decelerate when closer than such distance to the front vehicle, while they will maintain their actual distance if farther. $5\,\mathrm{m}$ is a typical inter-vehicle distance for the PATH CACC [19]. Observing the evolution of the virtual distance in Fig. 9a (ideal scenario) we see that both leaders are located too far ahead. Given the initial conditions of this simulation, leader B starts from a virtual distance of $0\,\mathrm{m}$ ($5\,\mathrm{m}$ below target), meaning that it needs to decelerate to leave room for platoon C to merge in, while leader C is $15\,\mathrm{m}$ below the target distance, i.e., it needs to decelerate to enter the intersection having the right distance to platoon A. The two platoons adapt their distance according to data received between them while adapting to the disturbances induced by the human-driven vehicle as well. When platoon C merges in the intersection at roughly $45\,\mathrm{s}$, leader B measures a negative distance spike due to platoon C entering the intersection. This just holds for a few moments,

Table I
COMMUNICATION PARAMETERS.

	Parameter	Value
802.11p	Path loss model	Free space ($\alpha = 2.0$)
	Shadowing model	Simple obstacle shadowing [30]
	PHY model	IEEE 802.11p
	MAC model	1609.4 single channel (CCH)
	Frequency	5.89 GHz, 10 MHz
	Bitrate	6 Mbit/s (QPSK R = 1/2)
	Transmit power	20 dBm
	Noise floor	−95 dBm
mmWave	Path loss model	Free space ($\alpha = 2.0$)
	Shadowing model	Simple obstacle shadowing [30]
	RIS model	Far field model derived from [26]
	PHY model	OFDM (IEEE 802.11a/g/p like)
	Frequency	25 GHz, 400 MHz
	Bitrate	120 Mbit/s (QPSK R = 1/2)
	Transmit power	30 dBm
	Noise floor	−80 dBm

i.e., till leader C communicates it has entered the intersection.

When enabling shadowing by buildings, we can see the information about the virtual distance missing for roughly 10 s in Fig. 9b. As leaders B and C are unable to communicate, they continue driving using data they received in the last message. By being both slightly off position they continue to decelerate trying to compensate for the error, but given that they are unable to communicate they find themselves way behind their optimal positions when they pass the building causing shadowing. The fact that the distance then decreases approaching the target is just due to the fact that the human-driven vehicle is decelerating when platoon C enters the intersection, as shown in Fig. 8b.

Notice that, in a scenario where vehicles cannot communicate for more than a couple of seconds, the maneuver should most probably be aborted for safety reasons. Here the maneuver continues to show the effects of communication impairments on vehicle dynamics.

The final graphs show the acceleration and the virtual distance profiles Fig. 8c and 9c when adding a mmWave interface supported by a RIS to the vehicles. By comparison with the ideal case, the two scenarios are undistinguishable. This means that, even in presence of a physical obstacle, vehicles are perfectly capable of communicating thanks to the help of the RIS. This shows the potential of RIS and mmWave applied to CD scenarios and maneuvering. The considered scenario is clearly a proof-of-concept, but the possibility of using mmWave to communicate "around the corner" will enable high-speed vehicle-to-vehicle communications (V2V) links, fundamental for future CD systems based on new paradigms such as CP.

V. CONCLUSIONS AND FUTURE WORK

In this paper we propose the use of RISs as an enabler for future cooperative driving maneuver in urban scenarios. We implement and validate a RIS model within the PLEXE framework, and we use such simulator to show the potential of RIS in a cooperative intersection merging maneuver. While being encouraging, the results are clearly preliminary, and there is several work ahead in order to properly measure the potential of this technology. This includes using more realistic channel models, measuring the actual data rate vehicles experience (fundamental for CP), considering tracking errors and RIS coding delays, as well as scheduling resources to enable a single RIS to serve multiple pairs of vehicles concurrently. The challenges ahead are numerous, but we are confident that this preliminary work can foster future research on this topic.

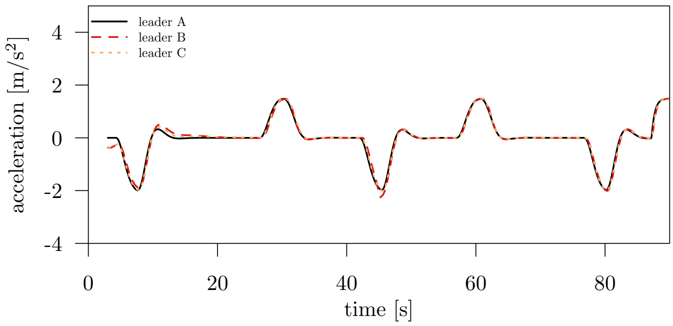

(a) 802.11p only, no shadowing

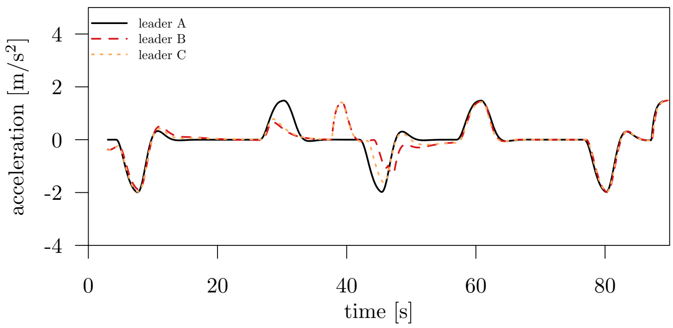

(b) 802.11p only, with shadowing

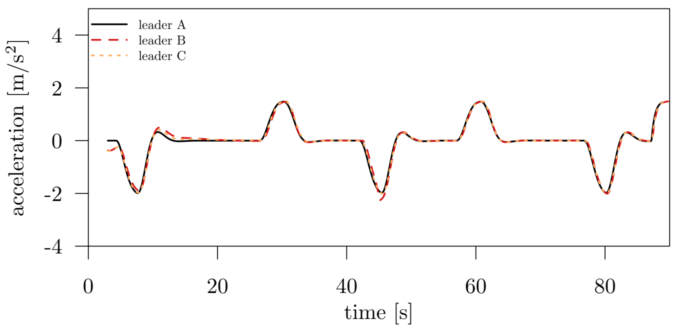

(c) 802.11p and mmWave with RIS, with shadowing

Figure 8. Acceleration profiles of the three platoon leaders.

REFERENCES

[1] M. Noor-A-Rahim, Z. Liu, H. Lee, et al., "6G for vehicle-to-everything (V2X) communications: Enabling technologies, challenges, and opportunities," *Proceedings of the IEEE*, 2022.

[2] X. Huang, D. Zhao, and H. Peng, "Empirical study of DSRC performance based on safety pilot model deployment data," *IEEE Transactions on Intelligent Transportation Systems*, vol. 18, no. 10, pp. 2619–2628, 2017.

[3] S. Wang, J. Huang, and X. Zhang, "Demystifying millimeter-wave V2X: Towards robust and efficient directional connectivity under high mobility," in *Proceedings of the 26th Annual International Conference on Mobile Computing and Networking*, 2020.

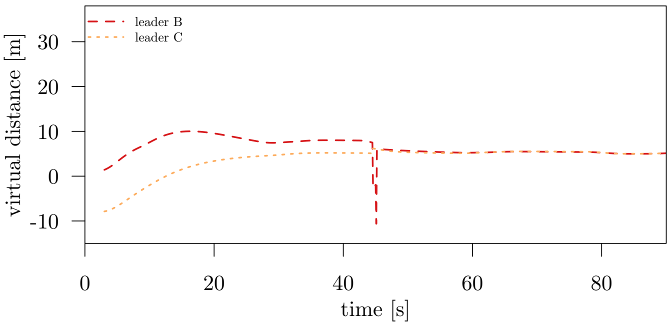

(a) 802.11p only, no shadowing

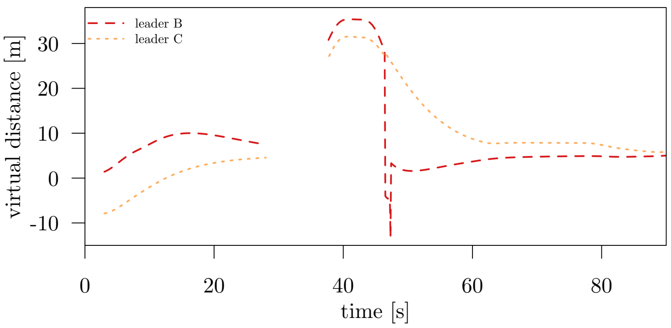

(b) 802.11p only, with shadowing

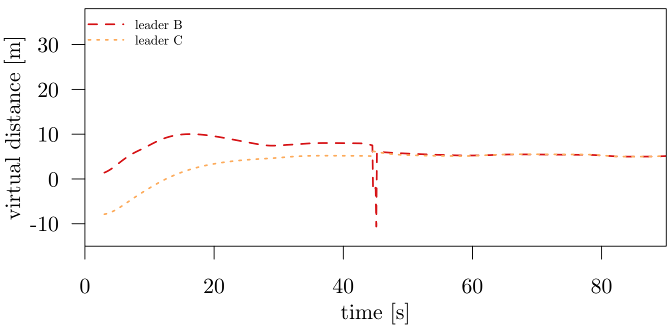

(c) 802.11p and mmWave with RIS, with shadowing

Figure 9. Virtual measured distances (platoon C leader to platoon A last member and platoon B leader to platoon C last member).

[4] C. Liaskos, S. Nie, A. Tsioliaridou, et al., "A New Wireless Communication Paradigm through Software-Controlled Metasurfaces," *IEEE Communications Magazine*, vol. 56, no. 9, pp. 162–169, 2018.

[5] D. Tyrovolas, S. A. Tegos, E. C. Dimitriadou-Panidou, et al., "Performance Analysis of Cascaded Reconfigurable Intelligent Surface Networks," *IEEE Wireless Communications Letters*, 2022.

[6] S. Nagata, "Trends and Target Implementations for 5G evolution & 6G," 2021.

[7] S. A. Tegos, D. Tyrovolas, P. D. Diamantoulakis, C. K. Liaskos, and G. K. Karagiannidis, "On the Distribution of the Sum of Double-Nakagami-m Random Vectors and Application in Randomly Reconfigurable Surfaces," *IEEE Transactions on Vehicular Technology*, vol. 71, no. 7, pp. 7297–7307, 2022.

[8] A. Pitilakis, O. Tsilipakos, F. Liu, et al., "A multi-functional reconfigurable metasurface: Electromagnetic design accounting for fabrication aspects," *IEEE Transactions on Antennas and Propagation*, vol. 69, no. 3, pp. 1440–1454, 2020.

[9] Q. Wang, Y. K. Liu, G. C. Wang, W. X. Jiang, and T. J. Cui, "Tunable triple-band millimeter-wave absorbing metasurface based on nematic liquid crystal," *AIP Advances*, vol. 12, no. 1, p. 015 127, 2022.

[10] Y. Zhu, B. Mao, and N. Kato, "Intelligent Reflecting Surface in 6G Vehicular Communications: A Survey," *IEEE Open Journal of Vehicular Technology*, vol. 3, pp. 266–277, 2022.

[11] Y. Chen, Y. Wang, and L. Jiao, "Robust Transmission for Reconfigurable Intelligent Surface Aided Millimeter Wave Vehicular Communications With Statistical CSI," *IEEE Transactions on Wireless Communications*, vol. 21, no. 2, pp. 928–944, 2022.

[12] J. Wang, W. Zhang, X. Bao, T. Song, and C. Pan, "Outage Analysis for Intelligent Reflecting Surface Assisted Vehicular Communication Networks," in *GLOBECOM 2020 - 2020 IEEE Global Communications Conference*, 2020, pp. 1–6.

[13] J. Nolan, K. Qian, and X. Zhang, "RoS: passive smart surface for roadside-to-vehicle communication," in *Proceedings of the 2021 ACM SIGCOMM 2021 Conference*, 2021, pp. 165–178.

[14] M. Ojaroudi, V. Loscrì, and A. M. Vegni, "Design and analysis of a reconfigurable intelligent meta-surface for vehicular networks," *ITU Journal on Future and Evolving Technologies*, Dec. 2020.

[15] Y. U. Ozcan, O. Ozdemir, and G. K. Kurt, "Reconfigurable Intelligent Surfaces for the Connectivity of Autonomous Vehicles," *IEEE Transactions on Vehicular Technology*, vol. 70, no. 3, pp. 2508–2513, 2021.

[16] T. Saeed, W. Aziz, A. Pitsillides, et al., "On the Use of Programmable Metasurfaces in Vehicular Networks," in *2021 IEEE 22nd International Workshop on Signal Processing Advances in Wireless Communications (SPAWC)*, 2021, pp. 521–525.

[17] Y. Ai, A. Felipe, L. Kong, M. Cheffena, S. Chatzinotas, and B. Ottersten, "Secure vehicular communications through reconfigurable intelligent surfaces," *IEEE Transactions on Vehicular Technology*, vol. 70, no. 7, pp. 7272–7276, 2021.

[18] K. Heimann, B. Sliwa, M. Patchou, and C. Wietfeld, "Modeling and Simulation of Reconfigurable Intelligent Surfaces for Hybrid Aerial and Ground-based Vehicular Communications," in *Proceedings of the 24th International ACM Conference on Modeling, Analysis and Simulation of Wireless and Mobile Systems*, 2021, pp. 67–74.

[19] M. Segata, R. Lo Cigno, T. Hardes, et al., "Multi-Technology Cooperative Driving: An Analysis Based on PLEXE," *IEEE Transactions on Mobile Computing (TMC)*, Feb. 2022, to appear.

[20] C. Sommer, R. German, and F. Dressler, "Bidirectionally Coupled Network and Road Traffic Simulation for Improved IVC Analysis," *IEEE Transactions on Mobile Computing (TMC)*, vol. 10, no. 1, pp. 3–15, Jan. 2011.

[21] R. Rajamani, H.-S. Tan, B. K. Law, and W.-B. Zhang, "Demonstration of Integrated Longitudinal and Lateral Control for the Operation of Automated Vehicles in Platoons," *IEEE Transactions on Control Systems Technology (TCST)*, vol. 8, no. 4, pp. 695–708, Jul. 2000.

[22] S. Kim, B. Qin, Z. J. Chong, et al., "Multivehicle Cooperative Driving Using Cooperative Perception: Design and Experimental Validation," *IEEE Transactions on Intelligent Transportation Systems (TITS)*, vol. 16, no. 2, pp. 663–680, Apr. 2015.

[23] R. Lo Cigno and M. Segata, "Cooperative driving: A comprehensive perspective, the role of communications, and its potential development," *Elsevier Computer Communications*, vol. 193, pp. 82–93, Sep. 2022.

[24] T. J. Cui, M. Q. Qi, X. Wan, J. Zhao, and Q. Cheng, "Coding metamaterials, digital metamaterials and programmable metamaterials," *Light: Science and Applications*, vol. 3, no. 10, Oct. 2014.

[25] H. Taghvaee, A. Jain, S. Abadal, G. Gradoni, E. Alarcón, and A. Cabellos-Aparicio, "On the Enabling of Multi-Receiver Communications With Reconfigurable Intelligent Surfaces," *IEEE Transactions on Nanotechnology*, vol. 21, pp. 413–423, 2022.

[26] H. Taghvaee, S. Abadal, A. Pitilakis, et al., "Scalability Analysis of Programmable Metasurfaces for Beam Steering," *IEEE Access*, vol. 8, pp. 105 320–105 334, May 2020.

[27] "3GPP, TR 138 901 - V15.0.0 - 5G; Study on channel model for frequencies from 0.5 to 100 GHz (3GPP TR 38.901 version 15.0.0 Release 15)," 2018.

[28] W. Tang, X. Chen, M. Z. Chen, et al., "Path Loss Modeling and Measurements for Reconfigurable Intelligent Surfaces in the Millimeter-Wave Frequency Band," *IEEE Transactions on Communications*, vol. 70, no. 9, pp. 6259–6276, Sep. 2022.

[29] N. Ashraf, M. Lestas, T. Saeed, et al., "Extremum Seeking Control for Beam Steering using Hypersurfaces," in *IEEE ICC 2020 Workshops*, Virtual Conference: IEEE, Jun. 2020.

[30] C. Sommer, D. Eckhoff, R. German, and F. Dressler, "A Computationally Inexpensive Empirical Model of IEEE 802.11p Radio Shadowing in Urban Environments," in *IEEE/IFIP WONS 2011*, Bardonecchia, Italy: IEEE, Jan. 2011, pp. 84–90.